Squirt flow due to interfacial water films in hydrate bearing sediments

Kathleen Sell[1†], Beatriz Quintal[2], Michael Kersten[1], and Erik H. Saenger[3,4]

[1] Johannes Gutenberg-University Mainz, Germany
[2] University of Lausanne, Switzerland
[3] International Geothermal Centre, Bochum University of Applied Sciences , Germany
[4] Ruhr University Bochum, Germany

[†] Corresponding author (sell@uni-mainz.de)

ABSTRACT

Sediments containing gas hydrate dispersed in the pore space are known to show a characteristic seismic anomaly which is a high attenuation along with increasing seismic velocities. Currently, this observation cannot be fully explained albeit squirt-flow type mechanisms on the microscale have been speculated to be the cause. Recent major findings from in-situ experiments, using the gas in excess and water in excess formation method, and coupled with high-resolution synchrotron-based X-ray micro-tomography, revealed a systematic presence of thin water films between the quartz grains and the encrusting hydrate. The data obtained from those experiments underwent an image processing procedure to quantify the thicknesses and geometries of the aforementioned interfacial water films. Overall, the water films vary from sub-µm to a few µm in thickness. In addition, some of the water films interconnect through water bridges. This geometrical analysis is used to propose a new conceptual squirt flow model for hydrate bearing sediments. A series of numerical simulations is performed considering variations of the proposed model to study seismic attenuation caused by such thin water films. Our results support previous speculations that squirt flow can explain high attenuation at seismic frequencies in hydrate bearing sediments, but based on a conceptual squirt flow model which is geometrically different than those previously considered.

Keywords: attenuation, squirt flow, interfacial films, dispersion, micro-tomography, gas hydrates, sediments, numerical modeling

1. INTRODUCTION

Important mechanisms of wave attenuation in fluid-saturated porous media from seismic to ultrasonic frequencies, include friction between grain boundaries (Winkler and Nur, 1982), global flow or Biot's mechanism (Biot, 1962), and wave-induced fluid flow at mesoscopic and microscopic scales (e.g., Müller et al., 2010). At the mesoscopic scale, patchy saturation and fractures are the most prominent causes of wave-induced fluid flow (White, 1975; White et al., 1975; Brajanovski et al., 2005; Tisato and Quintal, 2013; Quintal et al., 2014). At the microscopic scale, wave-induced fluid flow is commonly referred to as squirt flow and typically occurs between interconnected microcracks or between grain contacts and stiffer pores (O'Connell and Budiansky, 1977; Murphy et al., 1986; Mavko and Jizba, 1991; Sams et al., 1997; Adelinet et al., 2010; Gurevich et al., 2010). The attenuation caused by global flow as well as that caused by wave-induced fluid flow at microscopic or mesoscopic scales are frequency dependent. While the latter can have a strong effect at seismic frequencies (Pimienta et al., 2015; Subramaniyan et al., 2015; Chapman et al., 2016), global flow will only cause significant attenuation in reservoir rocks at ultrasonic frequencies or higher (e.g., Bourbie et al., 1987). The attenuation caused by friction between grain boundaries is, on the other hand, frequency independent and basically depends on the confining pressure and the strain imposed by the propagating wave (Winkler and Nur, 1982). Its effect is expected to be small for the correspondingly small strains caused by seismic waves used in exploration and reservoir geophysics. Furthermore, the attenuation caused by wave-induced fluid flow tends to be linearly superposed to that due to friction between grain boundaries, as shown by Tisato and Quintal (2014).

Gas hydrates (GH) are ice-like structures comprised of gas molecules entrapped by water molecules (Sloan and Koh, 2008). The widespread global occurrence of GH and the fact that 1 m^3 of GH contains up to 164 m^3 of natural gas (CH_4 and CO_2 at standard conditions) draws attention to the idea of using GH as a potential future energy resource (Schicks et al., 2011). Nevertheless, GH-bearing sediments have been discussed not only as a relatively clean hydrocarbon reservoir (Collett and Ladd, 2000), but also in terms of a geohazard that can potentially contribute to global warming associated to hydrate dissociation and subsequent destabilization of GH-cemented deep sea sediments at continental margins (Kvenvolden, 1993; Nixon and Grozic, 2007). Occurrences of GH are restricted to locations providing the required amount of gas and water and the preferred pressure-temperature (p/T) conditions, which are commonly referred to as the so-called gas hydrate stability zones. Usually, GH reservoirs are mainly limited to marine continental margins, deep lakes and permafrost regions (Bohrmann and Torres, 2006).

In the search for GH reservoirs, the attenuation of seismic waves caused by the pore fluids might be an important survey tool (e.g. Bellefleur et al. 2007). However, little effort has been directed toward studying its effects for unconsolidated sediments hosting GH in a rather dispersed manner. GH forming in the pore space of unconsolidated sediments at given p/T-conditions alters the effective elastic and effective transport properties of the hosting sediment. It is known that the presence of GH in the sediment not only reduces the porosity and causes significant changes on its permeability, but also results in higher P- and S-wave velocities due to stiffening of the hosting matrix (Dvorkin et al., 2003; Guerin & Goldberg, 2005; Yun et al., 2005; Priest et al., 2006; Waite et al., 2009). In other words, the bulk and shear moduli increase due to the GH matrix-supporting effect within the sedimentary frame (Ecker et al., 1998). Additionally, the presence of GH causes higher attenuation of the seismic waves (Bellefleur et al. 2007; Dewangan et al. 2014) which was in particular observed for sediments containing dispersed GH in the pore space (Guerin and Goldberg, 2002; Dvorkin and Uden, 2004). This anomalous seismic behavior in terms of increased attenuation and velocities (Guerin and Goldberg, 2002; Dvorkin and Uden, 2004) cannot be fully explained, although wave-induced fluid flow at the microscopic and mesoscopic scales have been speculated to cause them (Priest et al., 2006; Gerner et al. 2007). Gerner et al. (2007) conducted numerical P-wave velocity simulations in highly permeable sedimentary layers, similar to hydrate-bearing sediments, and identified interlayer flow at the mesoscopic scale (White et al., 1975) as a potential mechanism of attenuation. Other authors have considered classical squirt flow models (O'Connell and Budiansky, 1977; Murphy et al., 1986) as the main source of attenuation in hydrate-bearing sediments (Dvorkin and Uden, 2004; Guerin & Goldberg, 2005; Priest et al., 2006; Waite et al., 2009; Marin-Moreno et al., 2017).

Quantifying GH saturation levels through geophysical exploration techniques is, however, not straightforward as there are still open questions on GH formation, its microstructure and distribution in the natural settings. Additionally, the recovery of unaltered natural GH samples is hampered due to their fast decomposition under ambient conditions. Therefore, various researchers have attempted to mimic the natural environment of GH-bearing sedimentary matrices in laboratory experiments (Berge et al., 1999; Ecker et al., 2000; Dvorkin et al., 2003; Yun et al., 2005; Spangenberg and Kulenkampff, 2006; Priest et al., 2006, 2009; Best et al., 2010, 2013; Hu et al., 2010; Li et al., 2011; Zhang et al., 2011; Dai et al., 2012; Schicks et al., 2013). The results of this collective effort established a number of conceptual models for the role of GH embedded in its sedimentary matrix (Figure 1). Nevertheless, these approximations turned out to be still not satisfactory. Although it has been suggested that all hydrate habits known from laboratory investigation involving synthetic samples occur also in nature (Spangenberg et al. 2015), none of those simplified models can yield accurate predictions of GH saturations from field electric resistivity or seismic data alone (Waite et al., 2009; Dai et al., 2012).

Chaouachi et al. (2015) performed in-situ experiments based on different formation mechanisms, including the "water in excess" and the "gas in excess" method, to form gas hydrates in various sedimentary matrices. The in-situ experiments coupled with high-resolution synchrotron-based X-ray micro-tomography (SRXCT) yielded 3D images of sub-μm spatial resolution. Using the "gas in excess" method, the water present in the samples weds the grain surfaces and transforms into GH at the required pressure/temperature conditions. When hydrate is formed with the "water in excess method" the grains will also be water wet, but these very thin (sub-micron) hydrate films between the grains and the hydrate structure will only occur at very high GH saturations. The resulting 3D micro-tomography data revealed the systematic presence of interfacial water films between the pore-filling GH and the grains, independently of which formation method was used (gas in excess or water in excess method). The observed interfacial water films are occasionally interconnected via water bridges but also water pockets are embedded in the GH.

For this study, the SRXCT data presented by Chaouachi et al. (2015) underwent an image processing workflow in order to quantify the thicknesses of the thin interfacial water films. Based on the obtained results, we introduce a conceptual model for GH-bearing sediments to numerically study squirt flow. Our numerical simulations allow for the dispersion of the P-wave modulus and the frequency-dependent P-wave attenuation. The results demonstrate the high levels of seismic attenuation/dispersion that a range of variations of our conceptual model can cause. Additionally, our results support the suggestions that the estimation of GH saturation, for GH occurring in a rather dispersed manner, could be accomplished by using seismic wave attenuation as a tool for indirect geophysical quantification (Guerin and Goldberg, 2002; Priest et al. 2006; Best et al. 2013; Marin-Moreno et al., 2017).

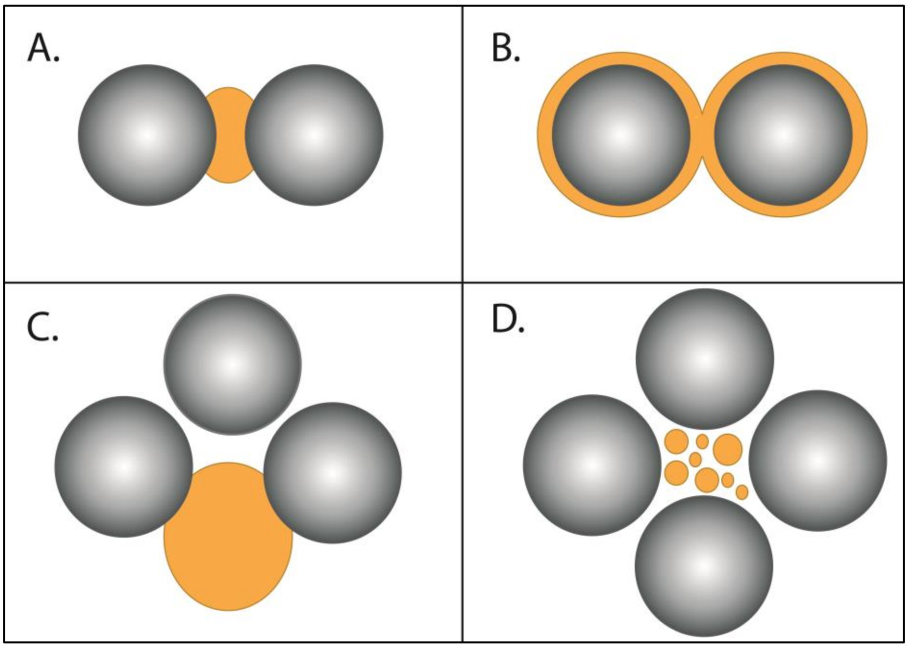

Figure 1. Review of the established conceptual models (Grains = grey and GH = orange), with (A) cementation – GH cements the grains, (B) encrustation – GH coats the grains, (C) matrix-supporting – GH is part of the sediment matrix, and (D) pore-filling – GH employs the pore space forming crystallites of varying size (modified after Dai et al., 2004).

2. THE INTERFACIAL WATER FILMS

Chaouachi et al. (2015) conducted various in-situ experiments coupled with synchrotron-based tomography at the TOMCAT beamline of the Paul Scherrer Institute in Villigen, Switzerland. The aim was to study the formation process and distribution of gas hydrates in various matrices, such as pure quartz sand and glass beads, as well as mixtures of quartz sand with clay minerals. These in-situ experiments have been conducted using an experimental setup that allowed for high pressures and low temperatures. Further details are given by Chaouachi et al. (2015), Falenty et al. (2015), and Sell et al. (2016).

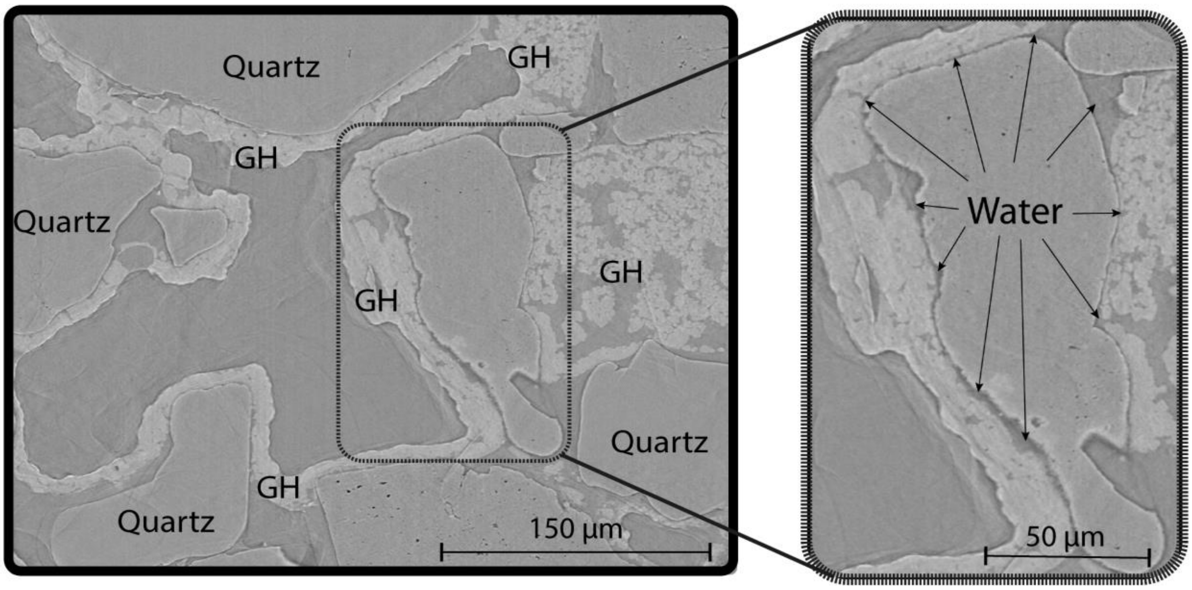

Figure 2. (Left) Overview of an unfiltered 2D slice in y,z-direction of quartz sand containing GH. Note that due to its unfiltered state, this image contains artifacts, such as streaks and slight edge enhancement. Phases can be identified on the base of grey scale differences.

For this study, the SRXCT data obtained from the mentioned in-situ experiments focused on samples containing pure natural quartz sand sieved at 200–300 µm grain size. Chuvilin et al. (2011) provides details on the sedimentology and mineralogy of the host sediment. We use a reconstruction process (Marone and Stampanoni, 2012) that yields an image matrix of 2560 × 2560 × 2160 voxels, with isometric voxel sizes of 0.74 and 0.38 µm at 10-fold and 20-fold optical magnification, respectively. The reconstructed tomograms revealed discernible grey value differences between the three relevant phases of the sample: solid grains, hydrate, and water (Figure 2). To reduce image artifacts, such as inhomogeneity in grey scale values, streaks and edge enhancement, we apply a systematic image enhancement workflow comprising different image filter combinations in 2D and 3D (Sell et al., 2016). Chaouachi et al. (2015) observed a systematic appearance of an interfacial water film separating the quartz grains from the GH phase in samples where GH was formed directly from the juvenile state not involving GH dissociation, as well as where GH was formed from the gas in excess method. This observation is in accordance with the publication of Tohidi et al. (2001). Additionally several molecular numerical simulations showed that a water layer prefers the interface of GH and quartz grains (Bagherzadeh et al., 2012; Bai et al., 2011; Liang et al., 2011). Identifying the water films and quantifying its thickness was one scope of this study to adapt our conceptual model.

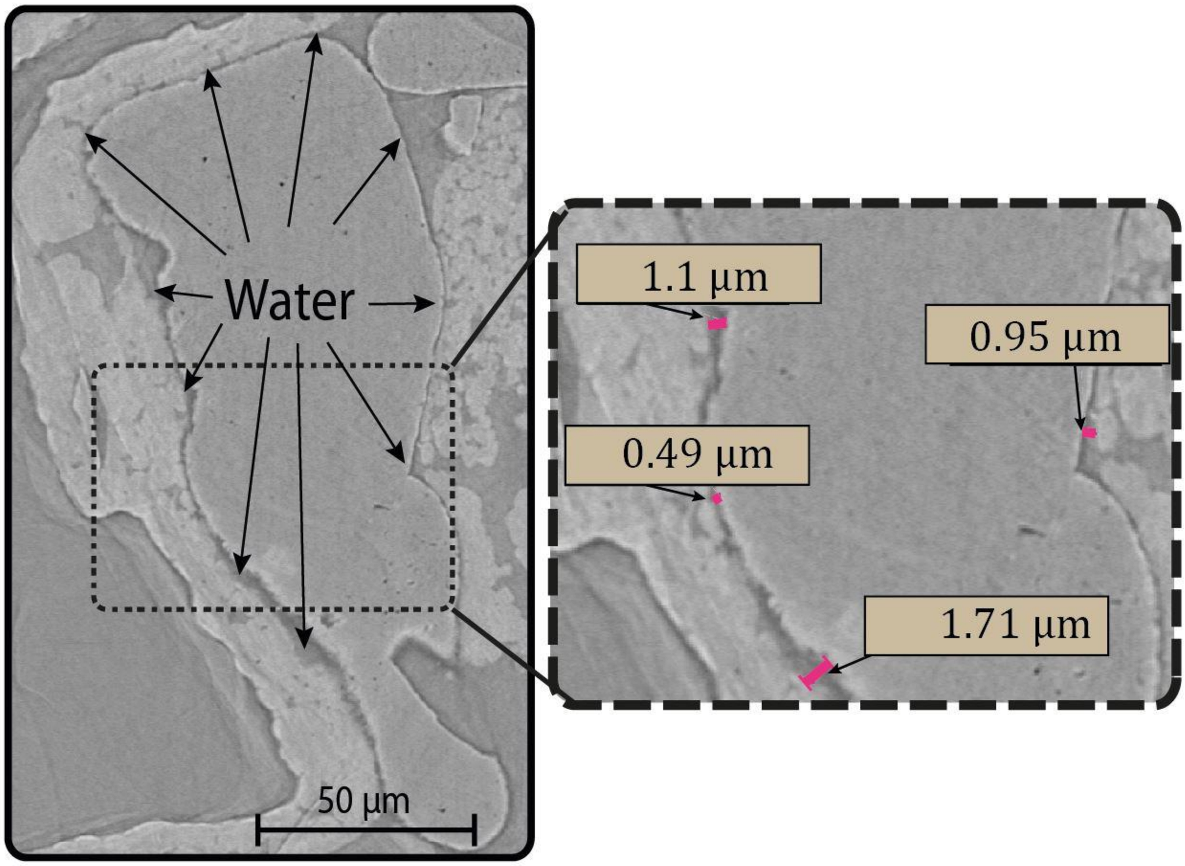

Figure 3. Raw (unfiltered) 2D image in y,z-direction at a spatial resolution of 0.38 m. The zoom depicts the measurement of a thin interfacial water film varying in thickness from 0.49 µm to 1.71 µm.

The broad range of grey scale values of the filtered images were classified using watershed segmentation combined with region growing tools of the software packages of Avizo Fire 7 (FEI, France) and Fiji. In the present study, we determined the thickness variation and geometry of the water film (Figure 3). Following the image enhancement and segmentation process described by Sell et al. (2016), the segmented data illustrate the characteristics and appearance of the phases distributed in the samples (Figure 4). Moreover, the high resolution of the data enables us to obtain 3D images in which particular details, such as water bridges connecting two interfacial water films, are detectable (Figure 5). With information collected from the 3D data, our proposed conceptual model involves round-shaped grains covered by a homogenous water film which is in turn embedded in non-porous hydrate. The conceptual model can be adjusted to include water bridges connecting the water films (Figure 6) and/or isolated water pockets within the hydrate and separated from the water films.

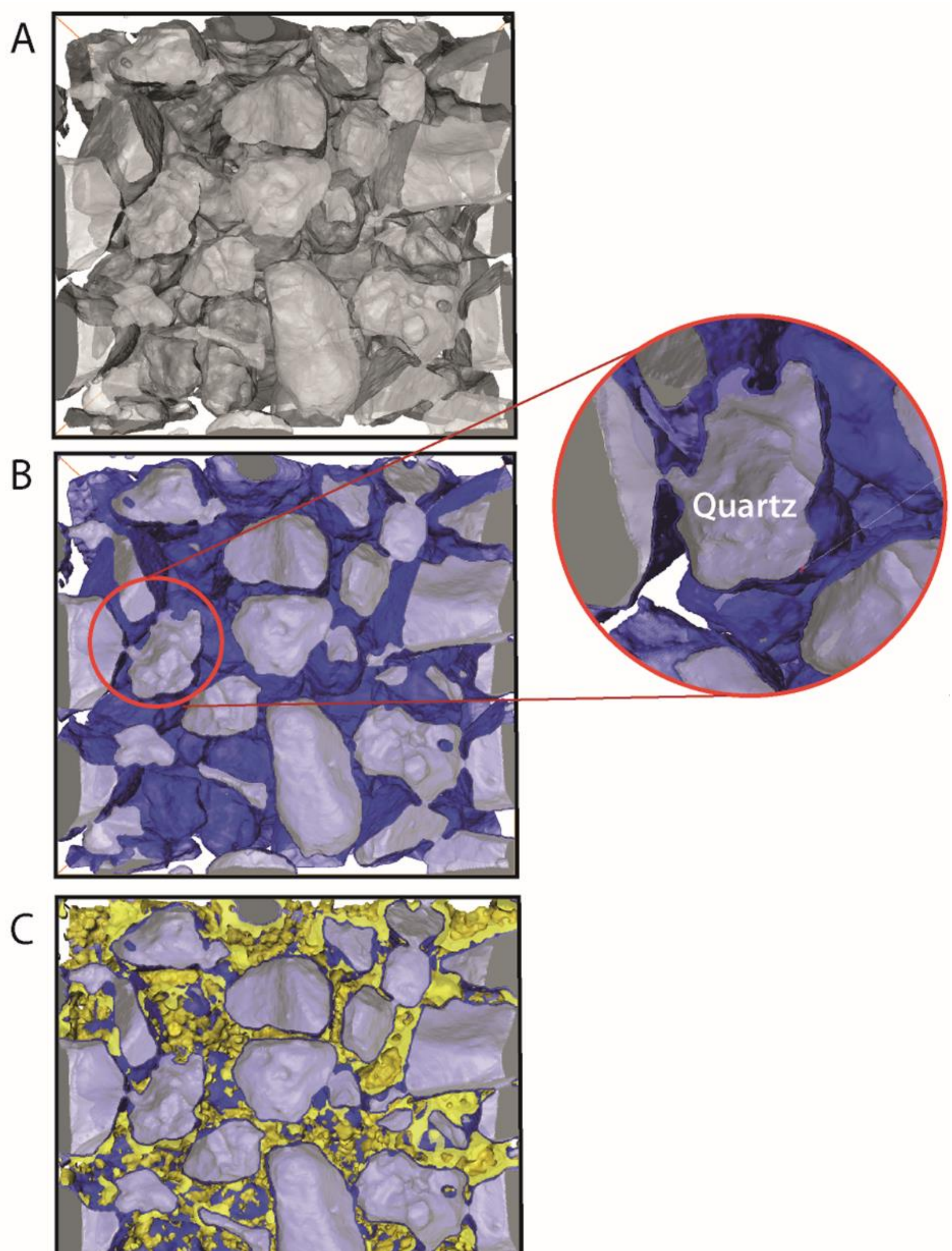

Figure 4. Volume-rendered phases in a representative image sample. For a better visualization, the phases are introduced step-by-step, with (A) grains (grey), (B) grains and interfacial water films (blue), and (C) grains, water film and hydrate (yellow). A zoom in (B) shows an interfacial water film measured at 1 – 4 voxels equivalent to 0.38 – 1.52 μm thickness, respectively.

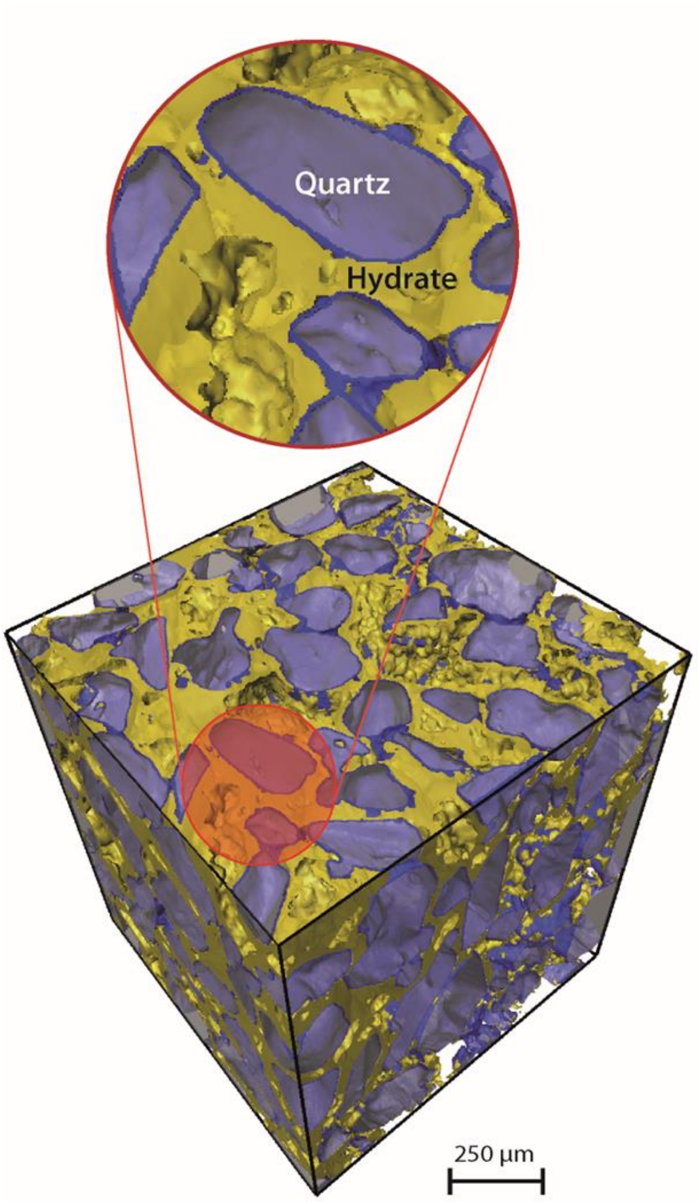

Figure 5. Volume-rendered image of a representative Region of interest (ROI) of 600 × 600 × 600 voxels at 0.38 μm spatial resolution. The zoom-in depicts quartz grains fully separated from the pore-filling hydrate by thin interfacial water films, with two quartz grains having their water films interconnected by a water bridge.

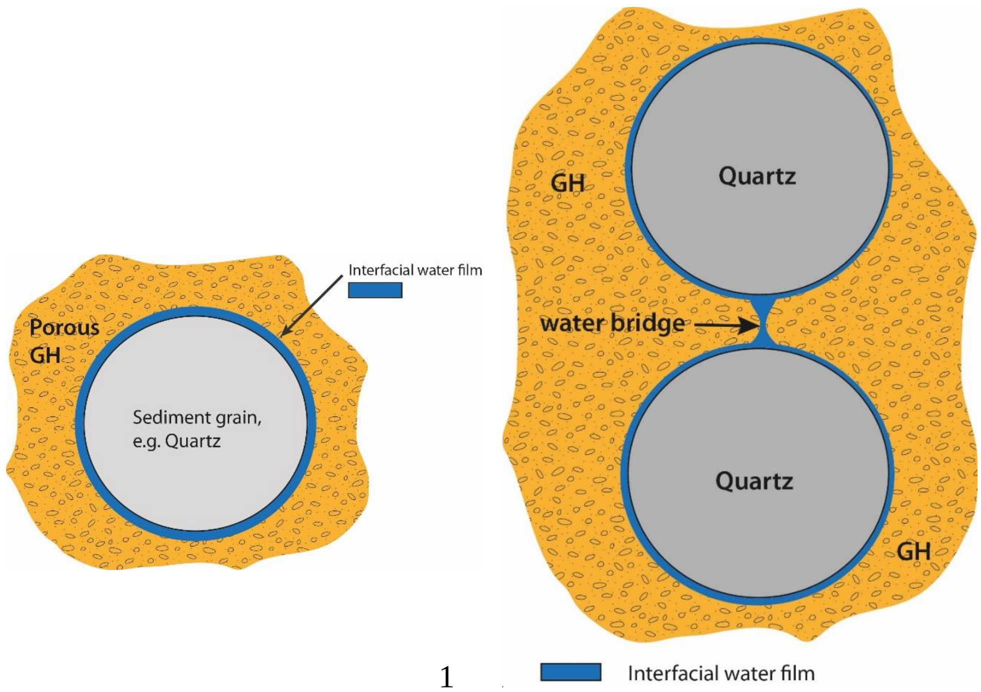

Figure 6. Schemes of (A) a new concept model for GH encrusting quartz grains separated by a thin interfacial water film and (B) connected by a water bridge.

3. NUMERICAL METHODOLOGY

3.1 Mathematical formulation

To estimate frequency-dependent attenuation in the GH systems described above we employ a hydromechanical approach (Quintal et al., 2016) based on the conservation of momentum

$$\nabla \cdot \boldsymbol{\sigma} = 0, \tag{1}$$

with the components σ_{kl} of the stress tensor $\boldsymbol{\sigma}$ defined according to the general stress-strain relations in the frequency domain

$$\sigma_{kl} = 2\mu\varepsilon_{kl} + \left(K - \frac{2}{3}\mu\right)e\delta_{kl} + 2\eta\omega i\varepsilon_{kl} - \frac{2}{3}\eta\omega ie\delta_{kl}, \tag{2}$$

where ε_{kl} denotes the components of the strain tensor, e denotes the cubical dilatation given by the trace of the strain tensor, ω is the angular frequency, and i represents the unit imaginary number. The indexes k, l = 1, 2, 3 refer to the three Cartesian directions x_1, x_2, x_3 or x, y, z and δ_{kl} is the Kronecker delta ($\delta_{kl} = 1$ for $k = l$ and $\delta_{kl} = 0$ for $k \neq l$). The material parameters μ, K, and η are the shear modulus, the bulk modulus, and the shear viscosity, respectively.

Using this general mathematical formulation (equations 1 and 2), a heterogeneous medium can be described as having an isotropic, linear elastic solid frame and fluid-filled cavities or pores, to which a specific choice of material parameters can be assigned. Equation 2 reduces to Hooke's law by setting the shear viscosity η to zero in the solid domains. In these regions, μ and K denote the shear and bulk moduli of the corresponding elastic solid. In the fluid-filled domains, the shear modulus μ is set to zero while K and η denote the bulk modulus and shear viscosity of the fluid. In this domains the combined equations 1 and 2 reduce to the quasi-static, linearized Navier-Stokes' equations for the laminar flow of a Newtonian fluid (e.g., Jaeger et al., 2007).

When the aforementioned heterogeneous medium is deformed, fluid pressure differences between neighbor regions induce fluid flow or, more accurately, fluid pressure diffusion, which in turn results in energy loss caused by viscous dissipation (Quintal et al., 2016). At the microscopic scale, this attenuation mechanism is commonly referred to as squirt flow (e.g., O'Connell and Budiansky, 1977; Murphy et al., 1986) and is the sole cause of attenuation in our simulations, as we neglected the inertial terms in equations 1 and 2.

3.2 Finite element modeling

Our 2D problem is equivalent to a 3D case under plain strain conditions, which means no strain outside the modeling plane is allowed to develop. For the corresponding simulations, we consider the directions x and y, to be in the modeling plane and direction z to be the one in which no displacement or displacement gradients can occur.

The numerical solution is based on a finite-element approach in the frequency domain. We employ an unstructured triangular mesh, which allows for an efficient discretization of slender heterogeneities having large aspect ratios, such as the thin interfacial water films, by strongly varying the sizes of the triangular elements (e.g., Quintal et al., 2014). A few elements across the thin interfacial water film are necessary to accurately capture the viscous dissipation in this region, while much larger elements are sufficient in the solid elastic domains. The sizes of smallest and largest elements in our meshes differ by 3 orders of magnitude.

To assess the P-wave attenuation and modulus dispersion caused by squirt-flow, we subject a rectangular numerical model to an oscillatory test. A sinusoidal downward displacement is applied homogeneously at the top boundary of the numerical model. At the bottom, the displacement in the (y) vertical direction is set to zero. At the lateral boundaries of the model, the displacement in the (x) horizontal direction is set to zero. From this test, we obtain the stress and strain fields, averaged over the entire model domain. The mean stress and strain are used to compute the complex-valued and frequency-dependent P-wave modulus corresponding to a wave propagating in the vertical direction. The real part of the P-wave modulus H is used to illustrate the P-wave modulus dispersion while the ratio between its imaginary and real parts is used to quantify the P-wave attenuation $1/Q_P$. The S-wave attenuation and dispersion can be evaluated in a similar manner by changing the boundary conditions to those of a simple-shear test (e.g., Quintal et al., 2012, 2014).

Similar to the 2D problem, the solution to our 3D problem is based on the application of an unstructured mesh with tetrahedral elements. The element sizes in our 3D meshes also vary by about 3 orders of magnitude.

4. NUMERICAL RESULTS

Many sources of squirt flow might coexist in unconsolidated sediments hosting GH, such as those resembling the conventional squirt flow models introduced by O'Connell and Budiansky (1977) for interconnected microcracks and by Murphy et al. (1986) for microcracks or grain contacts connected to spherical pores. Marin-Moreno et al. (2017) describes an integrated approach that combines the effects of some squirt flow models and other attenuation mechanisms. Here our objective diverges from that. We instead aim at studying the squirt flow phenomenon and the resulting frequency-dependent attenuation associated with a specific model, which is geometrically different from the mentioned conventional squirt flow models and is based on the thin interfacial water films. We thus neglect all other potentials sources of attenuation.

4.1 Attenuation mechanism in a thin interfacial water film

Our 2D numerical model domain corresponds to a fundamental block of a periodic distribution of unconsolidated circular quartz grains dispersed in a continuous GH background and separated from the latter by a thin interfacial water film (Figure 7). The subdomain representing the thin interfacial water film is described by the corresponding properties of this viscous fluid, while the other subdomains are described by properties of two different elastic solids, quartz and GH. These properties are given in Table 1 and the numerical mesh is shown in Figure 8. We consider thicknesses of the interfacial water film ranging from 0.1 μm to 1 μm as well as two grain diameters 150 and 250 μm for the 2D model. These values were chosen considering the sizes of the quartz grains used in the laboratory experiment from which the SRXCT data were obtained, which ranged from 150 to 300 μm, and the thicknesses of the interfacial water films observed in the data, ranging from 0.38 μm to 1.5 μm. Note that the thinnest interfacial water films observed were limited by the highest achieved spatial resolution of 0.38 μm. Despite this limitation, water film thicknesses below 0.38 μm have also been considered for our numerical analysis.

The numerical results are expressed as the real part of the P-wave modulus and the P-wave attenuation $1/Q_P$ (Figure 9). We observe that a decrease in the thickness of the interfacial water film causes the attenuation and dispersion curves to shift to lower frequencies. In fact, high attenuation values ($1/Q \sim 0.1$) are observed at seismic frequencies (~100 Hz) when the interfacial water film is as thin as 0.1 μm and the grain diameter is as large as 250 μm. Decreasing the grain diameter causes a shift to higher frequencies of the attenuation and dispersion curves.

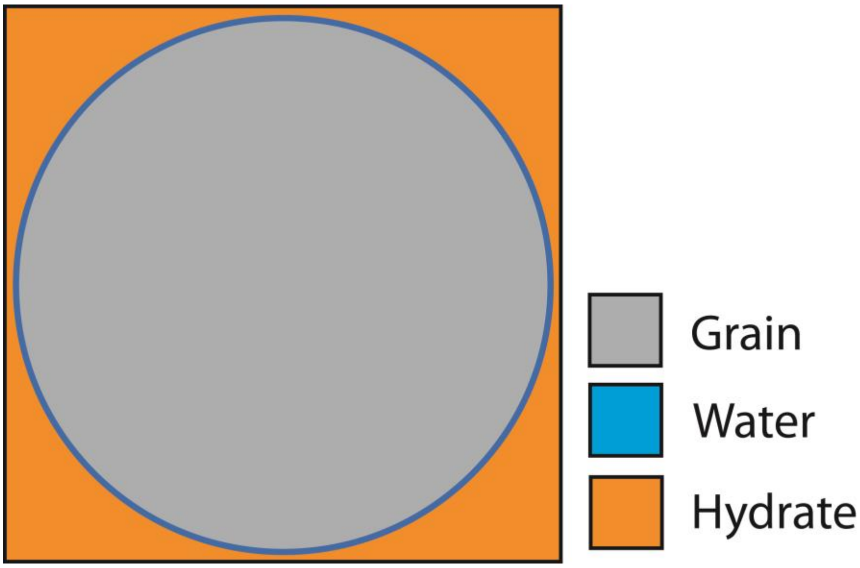

Figure 7. Fundamental block of an idealized periodic medium representing sediment grains which are separated from the embedding GH background by a thin interfacial water film.

Table 1. Material properties used in the numerical simulations. The properties of quartz are based on the work of Bass (1995) and those of hydrate on Helgerud (2003).

Material parameter	Quartz	Hydrate	Water
Shear modulus μ	44.3 GPa	13.57 GPa	0
Bulk modulus K	37.8 GPa	8.76 GPa	2.4 GPa
Shear viscosity η	0	0	0.003 Pa×s

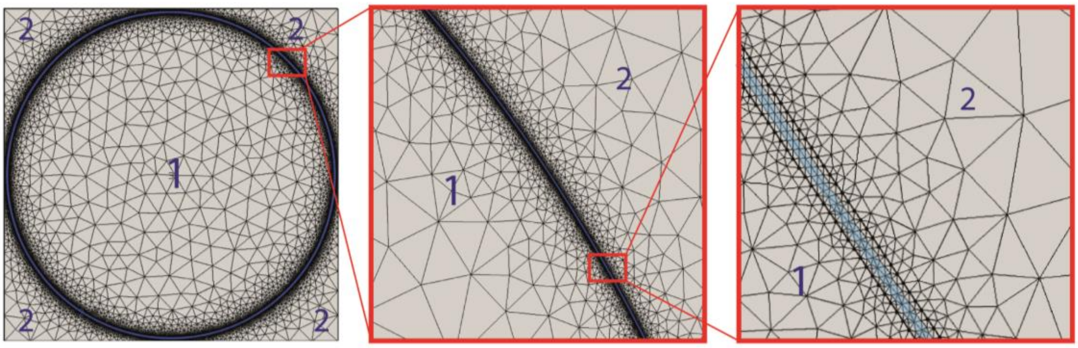

Figure 8. The triangular mesh used for the numerical model shown in Figure 7. To distinguish between the phases: Quartz is denoted with # 1,GH is denoted with # 2 and the interfacial water film is depicted in a light-blue color.

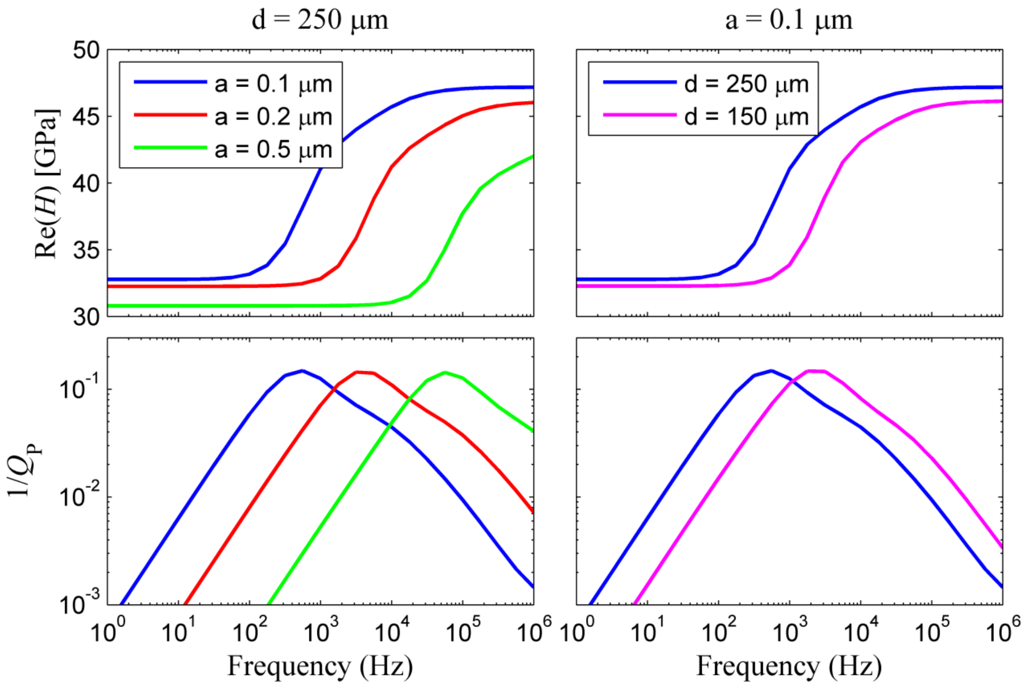

Figure 9. Real part of P-wave modulus, H, and corresponding P-wave attenuation, $1/Q_P$, as functions of frequency, for the model shown in Figure 7, considering the grain diameter d and thickness a of the interfacial water film, which are indicated in the legends and plot titles.

The geometry of the introduced model (Figure 7) is different than the classical squirt-flow geometries involving interconnected plane cracks or a plane crack connected to a pore of low aspect ratio. To better understand how dissipation occurs for this type of geometry, we initially focus on the fluid pressure field P (Figure 10) in the circular interfacial water film at the characteristic frequency. The vertical compression of the model illustrated in Figure 7 causes a larger deformation of the interfacial water film at the top and bottom parts than on the lateral parts. This observation is comparable to horizontal cracks that are more deformed by a vertical compression than vertical cracks in a classical squirt flow model. Here, the heterogeneous deformation causes fluid pressure to increase. The most deformed parts which are the top and the bottom, exhibit the highest fluid pressure, as shown in Figure 10. The pressure gradient present in this heterogeneous pressure field induces fluid to be displaced from the regions of higher pressure (top and bottom) towards the regions of lower pressure (left and right). The components of the fluid velocity field in the *x* and *y* directions V_x and V_y (Figure 11) and the corresponding local attenuation field 1/*q* (Figure 12) are depicted only the top-right quadrant of the model. Considering the symmetry of this process in the four quadrants of the circular interfacial water film (Figure 10) it is sufficient to show only one quadrant.

In Figure 11 we observe the text-book (e.g., Jaeger et al., 2007) parabolic profile of the fluid velocity across the interfacial water film, with larger fluid velocity in the center of the film, governed by Navier-Stokes equations. This fluid velocity is associated with an energy dissipation caused by viscous friction, shown in Figure 12. At the boundaries of the interfacial water film, larger viscous friction explains the lower fluid velocity and larger energy dissipation, in comparison to the center of the film. The attenuation is strongly reduced towards the center of the film by a few orders of magnitude. Looking at how these fields change along the interfacial water film, we observe that the maximal velocity and attenuation (compare Figures 11 and 12) coincide with the maximal pressure gradient (Figure 10). On the other hand, in the middle of the higher pressure and lower pressure regions, the pressure gradient is minimal causing the fluid velocity and attenuation to drop drastically.

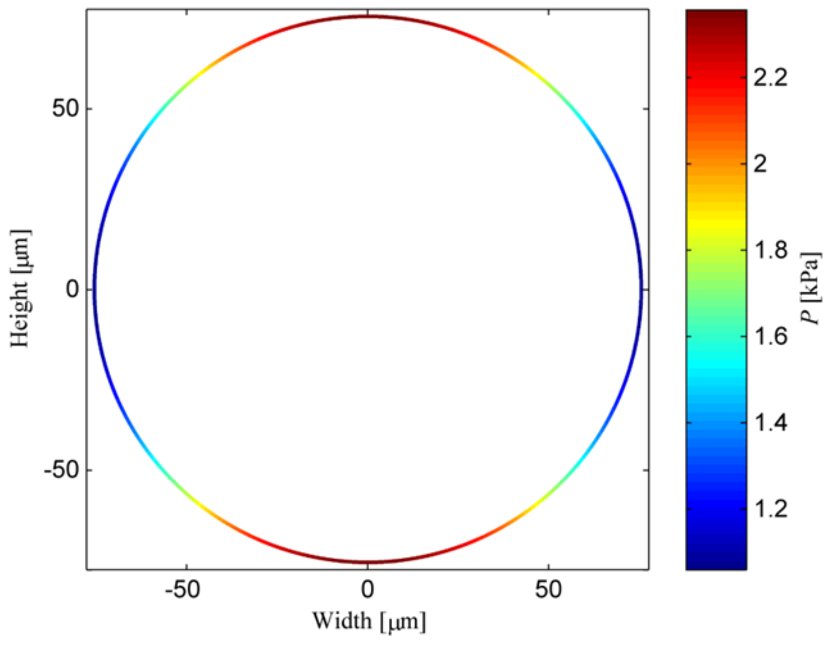

Figure 10. Fluid pressure *P* for the model shown in Figure 7, considering a grain diameter d = 150 μm and thickness of the interfacial water film a = 1 μm. The oscillation frequency is equal to the characteristic frequency (1.8×10^6 Hz).

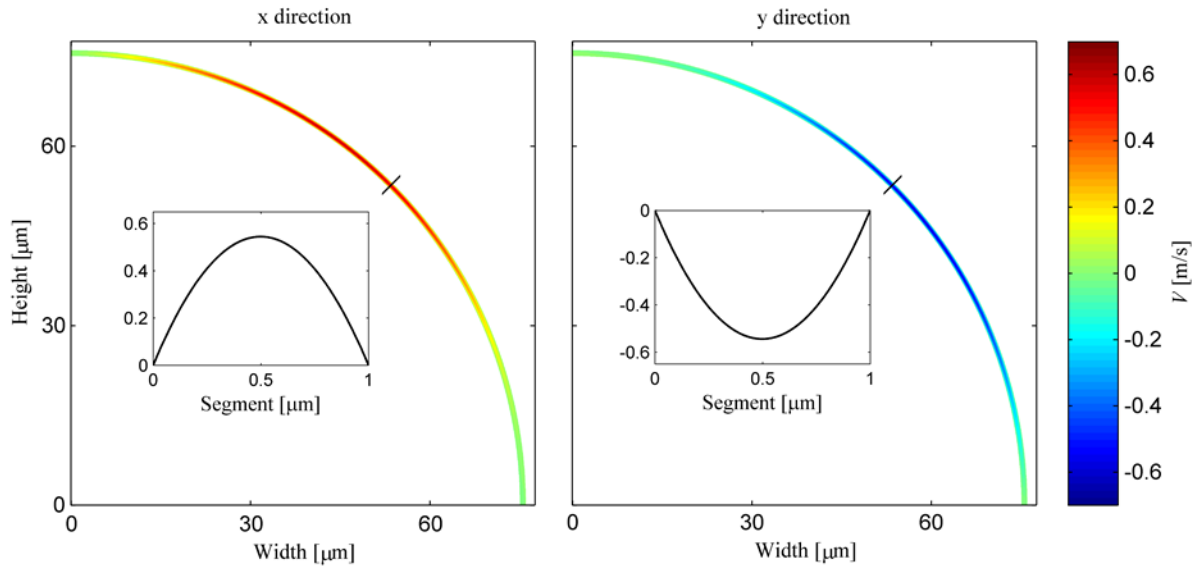

Figure 11. Zoom-in to the top-right quadrant of the model shown in Figure 9 showing the fluid velocity components V_x and V_z, for a grain diameter d = 150 μm, a thickness of the interfacial water film a = 1 μm, and at the characteristic frequency. These fields correspond to the fluid pressure field shown in Figure 10. The insets illustrate the profiles across the interfacial film where it is crossed by a black line.

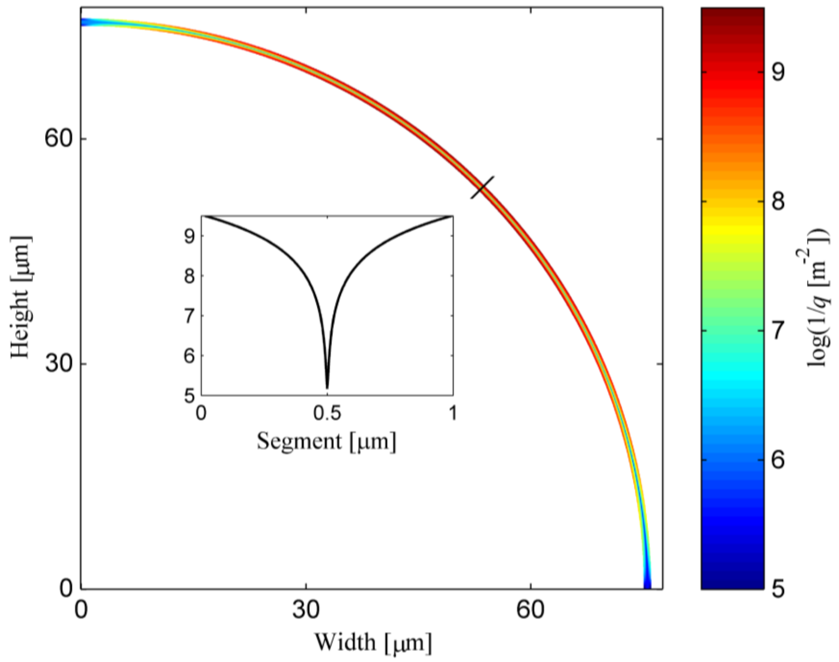

Figure 12. Zoom-in to the top-right quadrant of the model shown in Figure 7 showing the local attenuation 1/*q*, for a grain diameter d = 150 μm, with a water film thickness a = 1 μm, and at the characteristic frequency. This field corresponds to those shown in Figures 10 and 11. The inset illustrates the profile across the interfacial film where it is crossed by a black line.

4.2 Effects of water pockets and water bridges

In this subsection, a few alterations are added to the basic model illustrated in Figure 7. These alterations base on more detailed observations obtained from SRXCT, such as water pockets in non-porous GH or a water bridge that might occur connecting two neighboring interfacial water films (Figure 13). For this, the effect of these features on the P-wave modulus dispersion and attenuation (Figure 14) is studied and compared to results obtained from corresponding models where these features have not been considered.

The inclusion of water pockets has a modest effect on the attenuation and dispersion, while it reduces the overall value of the P-wave modulus, as a certain volume of GH is replaced by a much less stiff material (water). The modest increase in attenuation is associated with a more compressible effective background; no attenuation occurs within the water pockets.

The connecting water bridge introduces an additional length scale for the dissipation process, as fluid flow and dissipation will also occur through this relatively short and wide path. This explains the additional attenuation peak observed at higher frequencies, while the previous peak at 2×10^3 Hz suffers a slight reduction in magnitude. A reduction in magnitude occurs because the pressure equilibration process involving the water bridge causes a reduction in pressure in the region connected to the bridge and thus a reduction of the previously discussed (Figure 9) pressure gradient between this region and the sides of the circular interfacial water film. The dispersion agrees with the attenuation curve, with two inflections corresponding to the two attenuation peaks between the high- and low-frequency limits.

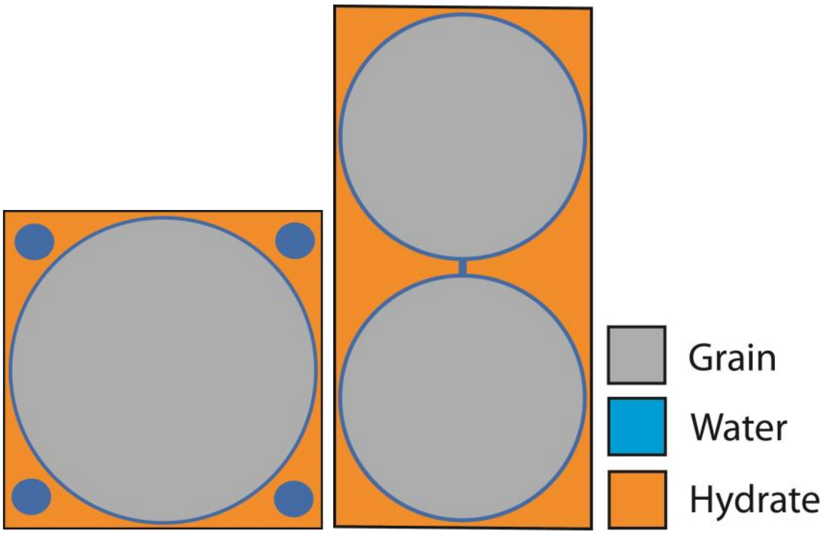

Figure 13. Fundamental blocks of two periodic media representing loose sandstone grains which are separated from the embedding GH background by a thin interfacial water film. On the left water pockets are located in the GH background and on the right the interfacial water films are connected to another through a water bridge**.**

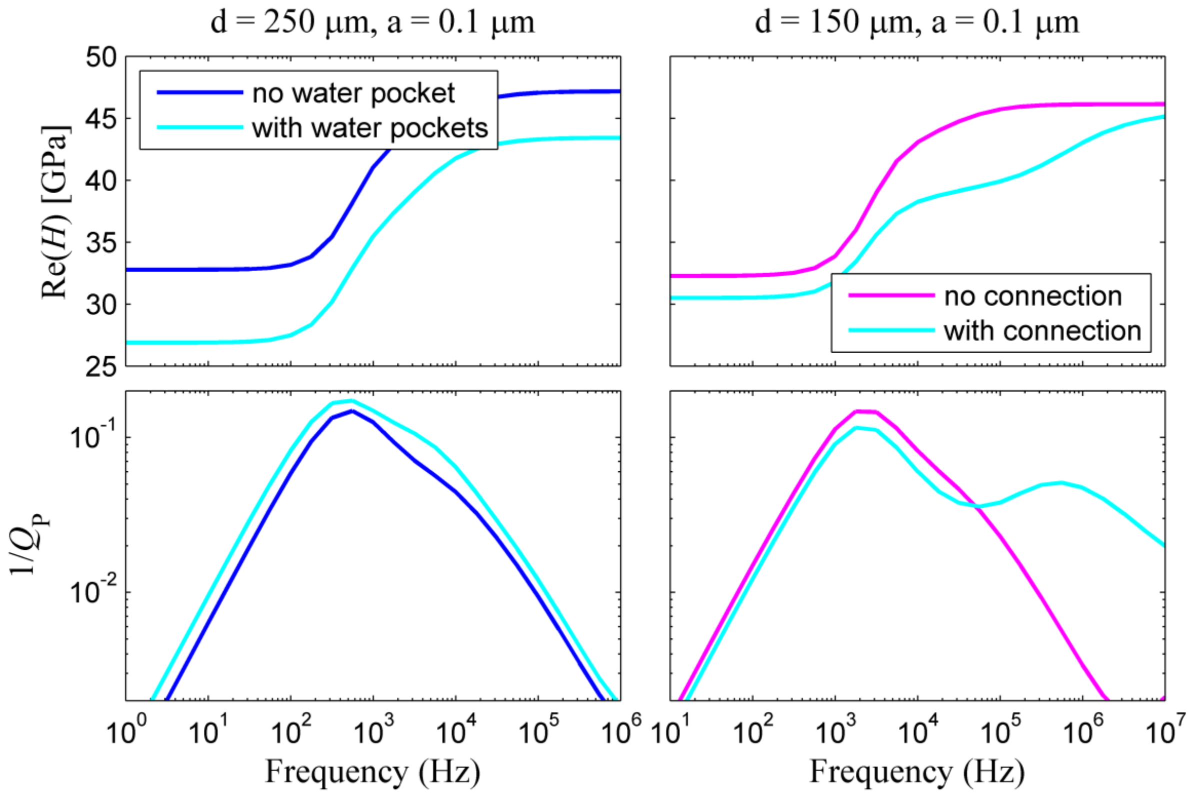

Figure 14. Real part of P-wave modulus, H, and corresponding P-wave attenuation, $1/Q_P$, as functions of frequency, for the models shown in Figure 13 in comparison with the corresponding results from the model shown in Figure 7 and given in Figure 9. The grain diameter d and thickness a of the interfacial water film are indicated in the plot titles.

4.3 Evaluation of 3D effects

This subsection considers a comparison between the results of the simulation illustrated in Figures 10-12, for the 2D model shown in Figure 7, and those of a simulation performed on its 3D counterpart. Our 3D model consists of a sphere in the middle of a cube (Figure 15), for which a centered cross section matches the 2D model shown in Figure 7. The thickness of the water film is 1 μm and the grain diameter is 150 μm (as for Figures 10-12). The numerical results are shown in Figure 16 with an excellent agreement between the results from the 2D and 3D models in terms of magnitude and characteristic frequency of attenuation. Indeed this was expected due to the radial symmetry of the spherical interfacial water film. This outcome indicates that 3D effects are small for the adopted geometry. The results based on simple 2D models approximate well the dissipation magnitude and frequency dependence of their corresponding 3D scenarios. The difference in the overall value of the real-valued P-wave modulus is associated with a larger relative quantity of soft GH and a lower relative quantity of stiff quartz in the 3D model.

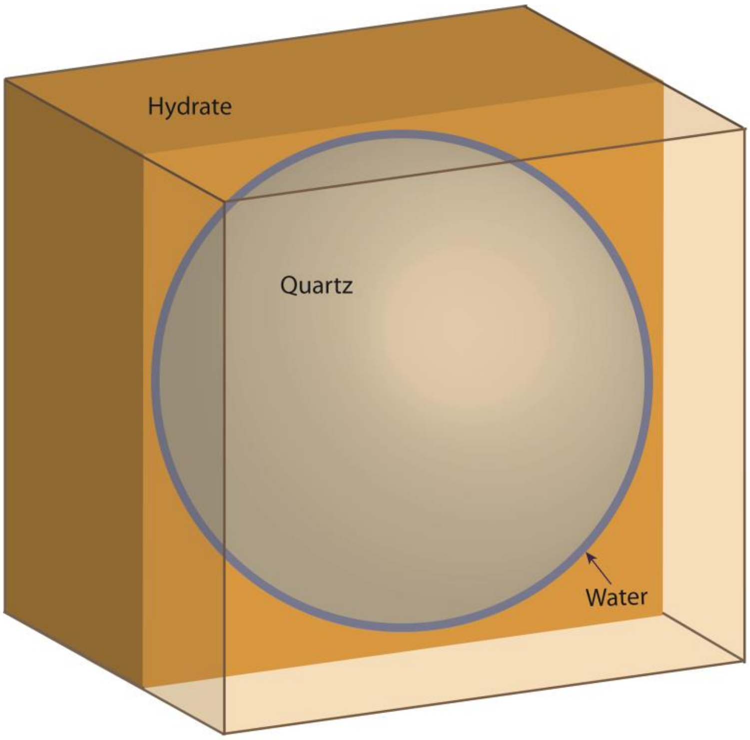

Figure 15: The 3D counterpart of the model shown in Figure 7: Fundamental block of a periodic medium representing unconsolidated quartz grains which are separated from the embedding GH background by a thin interfacial water film.

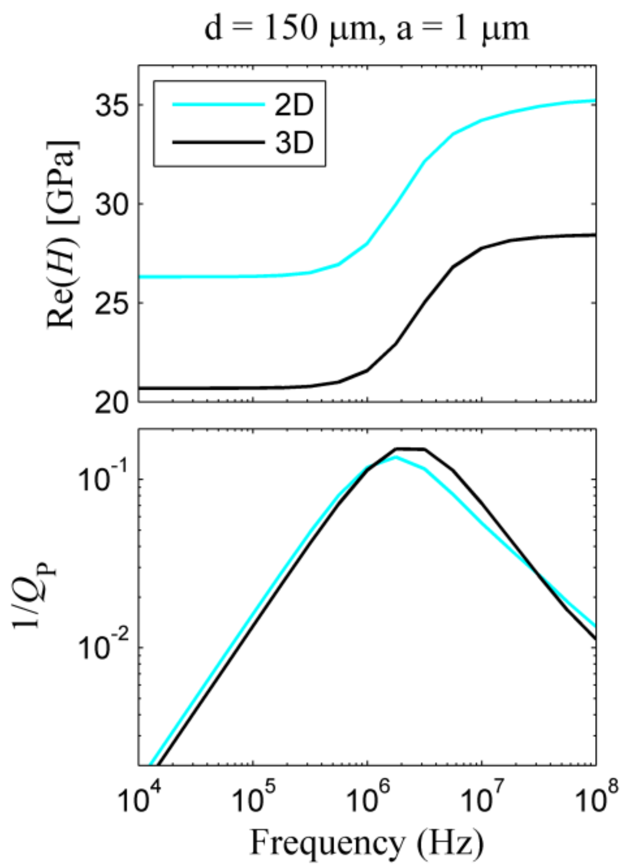

Figure 16. Real part of P-wave modulus, H, and corresponding P-wave attenuation, $1/Q_P$, as functions of frequency, for the 2D model shown in Figure 7 and for its 3D counterpart shown in Figure 15. The grain diameter d and thickness a of the interfacial water film are indicated in the plot title. The fields shown in Figures 10-12 correspond to this 2D simulation.

5. CONCLUSIONS

Interfacial water films between sediment grains and the embedding GH matrix were recently observed in GH-bearing sediments through synchrotron-based micro-tomography at a spatial resolution down to 0.38 μm. Based on these data, we have determined the appearance and thicknesses of such films. With this knowledge, a new conceptual squirt flow model, which refers to a spherical water film coating the solid grains, was introduced for GH-bearing sediments. This geometry differs from the classical squirt flow models involving microcracks, interconnected or connected to spherical pores. Numerical simulations were performed to calculate the energy dissipation in the proposed model, considering a range of scenarios. Our results show that squirt flow in spherical interfacial water films can cause large and frequency-dependent P-wave attenuation in a broad frequency range including seismic frequencies.

The numerical scheme is based on a set of coupled equations that reduce to Hooke's law in the subdomains of the model corresponding to the elastic solid materials (grains and GH) and to the quasi-static, linearized Navier-Stokes equations in the subdomains corresponding to the fluid (water). The results for our conceptual model show that the P-wave attenuation peak is shifted to lower frequencies with decreasing thickness of the interfacial water film and with increasing grain size (or the length of the film), as analogously known for the microcrack aperture and length in classical squirt flow models. Furthermore, we tested the effect of inserting water pockets in an embedding GH matrix and the effect of connecting two neighboring interfacial water films through a water bridge. In general, the water bridges have a stronger effect on energy dissipation than the water pockets. Introducing such connections between neighboring interfacial water films causes a broadening of the P-wave attenuation spectrum towards higher frequencies. On the other hand, the presence of water pockets in the GH background only causes a slight overall increase in P-wave attenuation. Although the majority of our simulations were performed for 2D models, results of a 3D simulation showed that 3D effects are small for the basic 2D models that we have considered.

Our results represent a strong base to explain fundamental processes in GH-bearing sediments and support previous speculations (Guerin and Goldberg, 2002; Dvorkin and Uden, 2004, Priest et al., 2006) that squirt flow is an important attenuation mechanism in such media, even at frequencies as low as those in the seismic range. This strengthens the perception that P-wave attenuation may be used as an indirect geophysical attribute to estimate GH saturation. Nevertheless, further studies considering more realistic geometries for the microstructure of GH bearing sediments are necessary for a successful strategy to estimate GH saturations where hydrate is distributed in a dispersed manner instead of massive layers. This study represents the first attempt to understand P-wave attenuation in unconsolidated sediments having large GH saturations. For a following study, our aim is to implement the segmented 3D images obtained from synchrotron-based micro-tomography as a direct model input for numerical investigations whereby realistic grain-to-grain contacts will be taken into account. The step towards more realistic structures as a model input is challenging due to the corresponding large computational demand. Furthermore, such model input requires additional segmentation steps for the 3D images that allow for a smoothing of the stairs-like resolution artifacts at the boundaries of the interfacial water films.

ACKNOWLEDGEMENTS

The authors thank the staff of the GZG crystallography group headed by Prof. W.F. Kuhs of the Georg August University Göttingen for their collaboration during the in-situ experiments at the TOMCAT beamline (Paul Scherrer Institute in Villigen, Switzerland) in 2012 and 2013. The presented work was co-funded by the German Science Foundation (DFG grant Ke 508/20 and Ku 920/18).

REFERENCES

Adelinet, M., J. Fortin, Y. Guéguen, A. Schubnel, and L. Geoffroy (2010) Frequency and fluid effects on elastic properties of basalt: Experimental investigations: Geophysical Research Letters, 37, L02303, doi: 10.1029/2009GL041660.

Bagherzadeh, S. A., P. Englezos, S. Alavi, and J. A. Ripmeester (2012) Molecular modeling of the dissociation of methane hydrate in contact with a silica surface. J. Phys. Chem. B, 116, 3188–3197, Doi: 10.1021/jp2086544.

Bai, D., G. Chen, X. Zhang, and W. Wang (2011) Microsecond molecular dynamics simulations of the kinetic pathways of gas hydrate formation from solid surfaces. Langmuir, 27, 5961–5967, Doi:10.1021/la105088b.

Bass, J. D. (1995), Elasticity of Minerals, Glasses and Melts, In: Mineral physics and crystallography: a handbook of physical constants, edited by T. J. Ahrens, pp. 45-63, American Geophysical Union, Washington D.C., USA.

Berge, L. I., K. A. Jacobsen, and A. Solstad (1999), Measured acoustic wave velocities of R11 (CCl3F) hydrate samples with and without sand as a function of hydrate concentration, J. Geophys. Res.-Solid Earth, 104(B7), 15415-15424.

Bellefleur, G., M. Riedel, T. Brent, F. Wright, and S. R. Dallimore (2007), Implication of seismic attenuation for gas hydrate resource characterization, Mallik, Mackenzie Delta, Canada, J. Geophys. Res., 112, B10311, doi:10.1029/2007JB004976.

Best, A., J. Priest, and C. Clayton (2010), A Resonant Column Study of the Seismic Properties of Methane-Hydrate-Bearing Sand, in Geophysical Characterization of Gas Hydrates, edited by M. Riedel, E. C. Willoughby and S. Chopra, pp. 337-347, Society of Exploration Geophysicists.

Best, A. I., J. A. Priest, C. R. I. Clayton, and E. V. L. Rees (2013), The effect of methane hydrate morphology and water saturation on seismic wave attenuation in sand under shallow sub-seafloor conditions, Earth Planet. Sci. Lett., 368, 78-87.

Biot, M. A., 1962, Mechanics of deformation and acoustic propagation in porous media: Journal of Applied Physics, 33, 1482-1498, doi: 10.1063/1.1728759.

Bohrmann, G. T. M. E. (2006), Gas Hydrates in Marine Sediments, in Marine Geochemistry, edited, pp. 481-512, Springer Berlin Heidelberg.

Brajanovski, M., B. Gurevich, and M. Schoenberg, 2005, A model for P-wave attenuation and dispersion in a porous medium permeated by aligned fractures, Geophysical Journal Internationl, 163, 372–384, doi: 10.1111/j.1365-246X.2005.02722.x.

Chaouachi, M., A. Falenty, K. Sell, F. Enzmann, M. Kersten, D. Haberthür, and W. F. Kuhs (2015), Microstructural evolution of gas hydrates in sedimentary matrices observed with synchrotron X-ray computed tomographic microscopy, Geochemistry, Geophysics, Geosystems, 16(6), 1711–1722.

Chapman S., Tisato N., Quintal B., Holliger K. (2016), Seismic attenuation in partially saturated Berea sandstone submitted to a range of confining pressures. Journal of Geophysical Research - Solid Earth, 121(3):1664–1676, doi: 10.1002/2015JB012575.

Chuvilin, E. M., V. A. Istomin, and S. S. Safonov (2011), Residual nonclathrated water in sediments in equilibrium with gas hydrate Comparison with unfrozen water, Cold Reg Sci Technol, 68(1-2), 68-73.

Collett, T. S. a. L., John (2000), 19. Detection of gas hydrate with downhole logs and assessment of gas hydrate concentrations (saturations) and gas volumes on the Blake Ridge with electrically resistivity log data. Proceedings of the Ocean Drilling Program. Scientific Results, 164.

Dai, J., H. Xu, F. Snyder, and N. Dutta (2004), Detection and estimation of gas hydrates using rock physics and seismic inversion: Examples from the northern deepwater Gulf of Mexico, The Leading Edge, 23(1), 60-66.

Dai, S., J. C. Santamarina, W. F. Waite, and T. J. Kneafsey (2012), Hydrate morphology: Physical properties of sands with patchy hydrate saturation, J. Geophys. Res.-Solid Earth, 117, 12.

Dewangan, P., R. Mandal, P. Jaiswal, T. Ramprasad, and G. Sriram (2014), Estimation of seismic attenuation of gas hydrate bearing sediments from multi-channel seismic data: A case study from Krishna-Godavari offshore basin, Mar. Petrol. Geol., 58, 356–367.

Dvorkin, J., A. Nur, R. Uden, and T. Taner (2003), Rock physics of a gas hydrate reservoir, The Leading Edge, 22(9), 842-847.

Dvorkin, J. and Uden, R. (2004), Seismic wave attenuation in a methane hydrate reservoir, The Leading Edge, 23(8), 730-732.

Ecker, C., J. Dvorkin, and A.M. Nur (1998), Sediments with gas hydrates: Internal structure from seismic AVO, Geophysics 63(5), 1659-1669.

Ecker, C., J. Dvorkin, and A. M. Nur (2000), Estimating the amount of gas hydrate and free gas from marine seismic data, Geophysics, 65(2), 565-573.

Falenty, A., M. Chaouachi, S. H. Neher, K. Sell, J.-O. Schwarz, M. Wolf, F. Enzmann, M. Kersten, D. Haberthur, and W. F. Kuhs (2015), Stop-and-go in situ tomography of dynamic processes - gas hydrate formation in sedimentary matrices, Acta Crystallographica Section A, 71(a1), s154.

Gerner, A., Saenger, E. H., Shapiro, S. A. (2007), Attenuation of P-waves due to interlayer fluid flow in hydrate-bearing sediments, J. Geophys. Eng., 4(4), 394-403.

Gurevich, B., D. Makarynska, O. B. de Paula, and M. Pervukhina (2010), A simple model for squirt-flow dispersion and attenuation in fluid-saturated granular rocks, Geophysics, 75, N109-N120, doi: 10.1190/1.3509782.

Helgerud, M. B., Waite, W. F., Kirby, S. H., and Nur, A. (2003), Measured temperature and pressure dependence of vp and vs in compacted, polycrystalline si methane and sii methane-ethane hydrate., Can. J. Phys., 81, 47–53.

Hu, G. W., Y. G. Ye, J. Zhang, C. L. Liu, S. B. Diao, and J. S. Wang (2010), Acoustic properties of gas hydrate-bearing consolidated sediments and experimental testing of elastic velocity models, J. Geophys. Res.-Solid Earth, 115, 11.

Jaeger, J. C., N. G. W. Cook, and R. W. Zimmerman (2007), Fundamentals of rock mechanics, 4th ed., Blackwell Publishing.

Kvenvolden, K. A. (1993), Gas hydrates - geological perspective and global change Rev. Geophys., 31, 173.

Li, F. G., C. Y. Sun, Q. Zhang, X. X. Liu, X. Q. Guo, and G. J. Chen (2011), Laboratory Measurements of the Effects of Methane/Tetrahydrofuran Concentration and Grain Size on the P-Wave Velocity of Hydrate-Bearing Sand, Energy Fuels, 25(5), 2076-2082.

Liang, S., and P. G. Kusalik (2011), The mobility of water molecules through gas hydrates. J. Am. Chem. Soc., 133(6), 1870–1876, Doi: 10.1021/ja108434h.

Marín-Moreno, H., Sahoo, S. K.; Best, A. I. (2017), Theoretical modeling insights into elastic wave attenuation mechanisms in marine sediments with pore-filling methane hydrate, J. Geophys. Res. Solid Earth, 60(5).

Marone, F., and M. Stampanoni (2012), Regridding reconstruction algorithm for real-time tomographic imaging, Journal of Synchrotron Radiation, 19(6), 1029-1037.

Mavko, G., and D. Jizba (1991), Estimating grain-scale fluid effects on velocity dispersion in rocks, Geophysics, 56, 1940-1949, doi: 10.1190/1.1443005.

Müller, T. M., B. Gurevich, M. Lebedev (2010), Seismic wave attenuation and dispersion resulting from wave-induced flow in porous rocks – A review. Geophysics, 75, 75A147–75A164, doi: 10.1190/1.3463417.

Murphy, W. F., K. W. Winkler, and R. L. Kleinberg (1986), Acoustic relaxation in sedimentary rocks, dependence on grain contacts and fluid saturation, Geophysics, 51, 757–766, doi: 10.1190/1.1442128.

Nixon, M. F. a. Grozic, J.L. (2007), Submarine slope failure due to gas hydrate dissociation: a preliminary quantification, Canadian Geotechnical Journal, 44(3), 314 - 325.

O'Connell, R. J., and B. Budiansky (1977), Viscoelastic properties of fluid-saturated cracked solids, Journal of Geophysical Research – Solid Earth, 82, 5719-5735, doi: 10.1029/JB082i036p05719.

Pimienta, L., J. Fortin, and Y. Guéguen (2015), Bulk modulus dispersion and attenuation in sandstones, Geophysics, 80(2), D111-D127, doi: 10.1190/geo2014-0335.1.

Priest, J. A., A. I. Best, and C. R. I. Clayton (2006), Attenuation of seismic waves in methane gas hydrate-bearing sand, Geophys. J. Int., 164(1), 149-159.

Priest, J. A., E. V. L. Rees, and C. R. I. Clayton (2009), Influence of gas hydrate morphology on the seismic velocities of sands, J. Geophys. Res.-Solid Earth, 114, 13.

Quintal, B., R. Jänicke, J. G. Rubino, H. Steeb, and K. Holliger (2014), Sensitivity of S-wave attenuation to the connectivity of fractures in fluid-saturated rocks, Geophysics, 79, WB15-WB24, doi: 10.1190/geo2013-0409.1.

Quintal, B., J. G. Rubino, E. Caspari, and K. Holliger (2016), A simple hydromechanical approach for simulating squirt-type flow, Geophysics, 81, D335–D344, doi: 10.1190/geo2015-0383.1.

Sams, M. S., J. P. Neep, M. H. Worthington, and M. S. King (1997), The measurement of velocity dispersion and frequency-dependent intrinsic attenuation in sedimentary rocks, Geophysics, 62(5), 1456-1464, doi: 10.1190/1.1444249.

Schicks, J. M., Spangenberg, E.; Giese, R.; Steinhauer, B,; Klump, J,; Luzi, M, (2011), New Approaches for the Production of Hydrocarbons from Hydrate Bearing Sediments, Energies, 4(12), 151-172.

Schicks, J. S., Erik; Giese, R.; Luzi-Helbing, M.; Priegnitz, M.; Beeskow-Strauch, B. (2013), A Counter-Current Heat-Exchange Reactor for the Thermal Stimulation of Hydrate-Bearing Sediments, Energies, 6(6), 3002-3016.

Sell, K., Saenger, E.H., Falenty, A., Chaouachi, M., Haberthür, D., Enzmann, F., Kuhs, W.F., Kersten, M. (2016), On the path to the digital rock physics of gas hydrate-bearing sediments – processing of in situ synchrotron-tomography data, 7, p. 1243-1258,

Sloan, E. D., and C. A. Koh (2008), Clathrate hydrates of natural gases, Third edition, CRC Press, Boca Raton, USA.

Spangenberg, E., and Kulenkampff, J. (2006), Influence of methane hydrate content on electrical sediment properties, Geophys. Res. Lett., 33(24), 5.

Spangenberg, E. P., M.; Heeschen, K.; Schicks, J. M. (2015), Are Laboratory-Formed Hydrate-Bearing Systems Analogous to Those in Nature?, J. Chem. Eng. Data 60(2), 258-268.

Subramaniyan, S., B. Quintal, C. Madonna, and E. H. Saenger (2015), Laboratory-based seismic attenuation in Fontainebleau sandstone: Evidence of squirt flow, Journal of Geophysical Research – Solid Earth, 120, 7526-7535, doi: 10.1002/2015JB012290.

Tisato, N., and B. Quintal (2013), Measurements of seismic attenuation and transient fluid pressure in partially saturated Berea sandstone: evidence of fluid flow on the mesoscopic scale: Geophysical Journal International, 195(1), 342-351, doi: 10.1093/gji/ggt259.

Tisato, N., and B. Quintal (2014), Laboratory measurements of seismic attenuation in sandstone: Strain versus fluid saturation effects, Geophysics, 79, WB9-WB14, doi: 10.1190/geo2013-0419.1.

Tohidi, B., R. Anderson, M. B. Clennell, R. W. Burgass, and A. B. Biderkab (2001) Visual observation of gas-hydrate formation and dissociationin synthetic porous media by means of glass micromodels. Geology, 29(9), 867–870, Doi: 10.1130/0091-7613(2001).

Waite, W. F., et al. (2009), Physical properties of hydrate-bearing sediments, Rev. Geophys., 47, 38.

White, J. E., 1975, Computed seismic speeds and attenuation in rocks with partial gas saturation: Geophysics, 40, 224-232, doi: 10.1190/1.1440520.

White, J. E., N. G. Mikhaylova, and F. M. Lyakhovitskiy, 1975, Low-frequency seismic waves in fluid-saturated layered rocks: Izvestiya, Academy of Sciences, USSR. Physics of the Solid Earth, 11, 654-659.

Winkler, K. W., and A. Nur (1982). Seismic attenuation: Effects of pore fluids and frictional-sliding. Geophysics, 47, 1-15, doi: 10.1190/1.1441276.

Yun, T. S., F. M. Francisca, J. C. Santamarina, and C. Ruppel (2005), Compressional and shear wave velocities in uncemented sediment containing gas hydrate, Geophys. Res. Lett., 32(10), 5.

Zhang, Q., F. G. Li, C. Y. Sun, Q. P. Li, X. Y. Wu, B. Liu, and G. J. Chen (2011), Compressional wave velocity measurements through sandy sediments containing methane hydrate, Am. Miner., 96(10), 1425-1432.